AMERICAN ACADEMY OF OPHTHALMOLOGY®

Automated Cone Photoreceptor Detection in Adaptive Optics Flood Illumination Ophthalmoscopy

Sander Wooning,[1,2] Pam A.T. Heutinck, MD,[3,4] Kubra Liman,[3,4] Sem Hennekam,[1,3] Manon van Haute,[5,6] Filip van den Broeck, MD,[5,6] Bart Leroy, PhD, MD,[5,6] Danuta M. Sampson, PhD,[7,8] Danial Roshandel, MD, PhD,[7,8] Fred K. Chen, MD, PhD,[7,8] Daniel M. Pelt, PhD,[2] L. Ingeborgh van den Born, MD, PhD,[9] Virginie J.M. Verhoeven, MD, PhD,[3,10] Caroline C.W. Klaver, MD, PhD,[3,4,11,12] Alberta A.H.J. Thiadens, MD, PhD,[3] Marine Durand,[13] Nicolas Chateau,[13] Theo van Walsum, PhD,[1] Danilo Andrade De Jesus, PhD,[1,3,9,*] Luisa Sanchez Brea, PhD[1,3,9,*]

Purpose: To develop and validate a deep learning–based model for detecting cone photoreceptor cells in adaptive optics flood illumination ophthalmoscopy (AO-FIO).

Design: Healthy volunteer study.

Participants: A total of 36 healthy participants were included.

Methods: The imaging protocol consisted of 21 AO-FIO images per eye acquired with the rtx1 adaptive optics retinal camera (Imagine Eyes), 4° × 4° each with 2° overlap, imaging a retinal patch 4° nasal (N) to 12° temporal (T) and −5° inferior to 5° superior relative to the fovea. Each image was divided into patches of 128 × 128 pixels, with a 20-pixel overlap. A training set (625 patches) from 18 subjects (32 ± 12 years, 6 males and 12 females) was annotated by a single center, whereas the test set (54 patches) from 18 subjects (40 ± 16 years, 11 males and 7 females) was annotated by graders from 3 different institutions. The deep learning model, based on the U-Net architecture, underwent a parameter search using the tree-structured Parzen estimator.

Main Outcome Measures: The F1 score was used to determine both intragrader and intergrader agreements and to evaluate the model's performance compared with the automated detection by the manufacturer's software (AOdetect Mosaic).

Results: The average intragrader agreement was 0.85 ± 0.06 between 2°N and 2°T, followed by 0.83 ± 0.09 between 3 and 6°T, and 0.80 ± 0.10 between 7 and 10°T. The average intergrader agreement for the 3 centers was 0.84 ± 0.05, 0.79 ± 0.05, and 0.76 ± 0.06 at 2°N–2°T, 3–6°T, and 7–10°T, respectively. The best combination of hyperparameters based on the tree-structured Parzen estimator algorithm achieved an F1 score of 0.89 ± 0.04. The average agreement between the model and the graders was 0.87 ± 0.04, 0.85 ± 0.03, and 0.81 ± 0.03 at 2°N–2°T, 3°–6°T, and 7°–10°T, respectively. These values were higher than those between AOdetect's auto detection without manual correction and the graders (0.84 ± 0.05, 0.79 ± 0.03, and 0.68 ± 0.04, respectively). A reduction in cone density was noted at greater eccentricities, in line with previous research findings, and the model indicated variations in estimating cell density for individuals aged 18 to 30 compared with those aged ≥50 years.

Conclusions: The performance of the developed deep learning–based model, AO-FIO ConeDetect, was comparable to that of graders from 3 medical centers. It outperformed the manufacturers' software auto-detection, particularly at higher eccentricities (7°–10°T). Hence, the model could reduce the need for manual correction and enable faster cone mosaic analyses.

Financial Disclosure(s): Proprietary or commercial disclosure may be found in the Footnotes and Disclosures at the end of this article. *Ophthalmology Science 2025;5:100675 © 2024 by the American Academy of Ophthalmology. This is an open access article under the CC BY-NC-ND license (http://creativecommons.org/licenses/by-nc-nd/4.0/).*

The introduction of adaptive optics (AO) in ophthalmic care has resulted in retinal images with unprecedented cellular resolution. Originally designed for astronomy,[2] AO corrects optical aberrations by changing the shape of deformable mirrors to compensate for the distortions in the light path. Retinal high-resolution imaging using AO allows for noninvasive examination of individual photoreceptor cells and other retinal structures, potentially opening the door to new retinal biomarkers.[3–6] Adaptive optics has been applied to different retinal imaging modalities, such as OCT,[7,8] scanning laser ophthalmoscopy,[7,9] and OCT angiography.[7,10] In preclinical and clinical practice, one of the prevailing AO modalities is adaptive optics flood illumination ophthalmoscopy (AO-FIO), typically in the form of the rtx1 (Imagine Eyes), a CE-certified device.[11]

https://doi.org/10.1016/j.xops.2024.100675
ISSN 2666-9145/25

Adaptive optics flood illumination ophthalmoscopy has mainly found applications in imaging photoreceptors, vessels, and retinal lesions.[12] Lesion analysis has been particularly valuable for monitoring changes over time in conditions such as age-related macular degeneration.[5,13] Vascular parameters, including inner diameter, outer diameter, parietal thickness, wall cross-sectional area, and wall-to-lumen ratio, have been predominantly explored in systemic hypertension and diabetes.[14] However, the primary focus of AO-FIO has been photoreceptor counting and spatial analysis, allowing for the calculation of cone photoreceptor density (cones/mm^2). Investigations into phenotypes and cell quantification have revealed significant changes in patients with retinal diseases, even when photoreceptor abnormalities were barely visible on OCT images or color fundus photography or in those with normal visual function.[15–18]

Despite AO-FIO's potential to assess lesions at a microscopic level, previously only available through postmortem histological examination, one of the main factors that precludes the widespread adoption of this modality is the lack of standardized measurement parameters and terminology and proper validation of AO imaging.[12] While a few studies have proposed methods for the automatic segmentation of photoreceptor cells in AO imaging,[19–21] to the best of our knowledge, only 2 algorithms have been proposed for AO-FIO images: the tool that accompanies the rtx1, AOdetect Mosaic (Imagine Eyes), and MATADOR, a Matlab-based software tool.[22] AOdetect is a semiautomated tool, intended by the manufacturer as an aid for annotating cone cells and analyzing their distribution over small regions of interest.[23] Cone cells are detected automatically and shall be verified and manually corrected by the user. Density values evaluated at 2° to 8° using the semiautomated method aided by AOdetect in healthy populations were within the range of the reference data from histology by Legras et al.[24] However, the regions analyzed with AOdetect (80 × 80 pixels) are small compared with the AO-FIO images (1500 × 1500 pixels). This limited area may not fully represent the variability across the entire field of view, potentially leading to sampling bias and inaccurate assessments of cell density. This, combined with the need for manual correction, makes quantitative analyses time consuming.[25] In the case of MATADOR, a notable limitation is that, like AOdetect, the developed tool is not open source, thereby hindering the possibility of making modifications or adaptations to the existing software for specific needs (e.g., computing a different biomarker). Lastly, both options rely on traditional image processing methods, which have drawbacks in terms of processing speed and analysis of suboptimal images (e.g., those showing motion-induced blurriness or poor contrast).[26]

This work aims to address the shortcomings of AOdetect and the MATADOR tool by introducing and validating an open-source deep learning model for the automatic detection of cone photoreceptors in AO-FIO images at various eccentricities and over larger regions. We assessed the performance of the model by comparing the results with manual annotations from 3 different centers and at different eccentricities, as well as with the reference standard software (AOdetect).

Methods

In this section, the methodology of the project is detailed, starting with the description of the image acquisition protocol and how the data were selected for this study. Then, we present the annotation process, which was semiautomatic for the training set and fully manual for the test set. Lastly, we describe the training and evaluation process of the proposed model, AO-FIO ConeDetect. An overview of the processing steps followed in this study is depicted in Figure 1.

Data Acquisition and Curation

This research is part of the AO-VISION study (MEC−2022−0495) that received approval from the Medical Ethics Committee at Erasmus MC (METC Erasmus Medisch Centrum Rotterdam). A signed consent was obtained from each participant, who was informed about the study and the intended application of their data. Before any analysis, the data were anonymized. This research adhered to the tenets of the Declaration of Helsinki.

Healthy volunteers participated in the AO-VISION study and underwent AO imaging of both eyes at Erasmus MC. The AO-FIO images were acquired using the rtx1 retinal camera[11] (Imagine Eyes), which uses infrared illumination at a wavelength of 850 nm, providing a lateral resolution of approximately 1.6 μm.[27] Each individual AO-FIO retinal image covers a 4° × 4° field of view, or 1500 × 1500 pixels per image.

The AO-VISION image acquisition protocol consists of 2 parts, with all measurements given as fixation coordinates: (1) 2 rows (1° superior and −1° inferior) of 6 images (2° overlap), from 2° nasal (N) to 10° temporal (T) eccentricity, for imaging any changes that may occur from the mid-periphery to the macula; (2) 2 additional rows (3° superior and −3° inferior) of 3 images (2° overlap), from 2°N to 2°T eccentricity, to image the foveal and parafoveal region, as depicted in Figure 2. Additionally, the protocol begins with 1 macula-centered image (0°, 0°) to check the participants' preferred locus of fixation. In total, 21 images are acquired, with an average acquisition time of approximately 10 minutes per eye. The region from the macula to the T mid-periphery was chosen to avoid signal attenuation caused by large vessel shadows. Lastly, a fovea-centered OCT volume scan per eye was acquired and used to confirm that there were no retinal abnormalities.

From the original dataset, a total of 38 AO-FIO images (4° × 4°) were selected from 36 participants, where the included eye was randomly selected per participant while aiming to maintain an overall equal ratio between the left eye and right eye. These images were taken at a range of fixation coordinates, from 2°N to 10°T. All images were of high quality for cell counting, as confirmed through visual inspection. This ensured that the images did not contain large vessel shadows, motion artifacts, or other acquisition artifacts and provided a clear visualization of the individual cell mosaic. The 38 selected images were then randomly divided into training and test sets for algorithm development and subsequent validation. The demographics of the dataset are further described in Table 1.

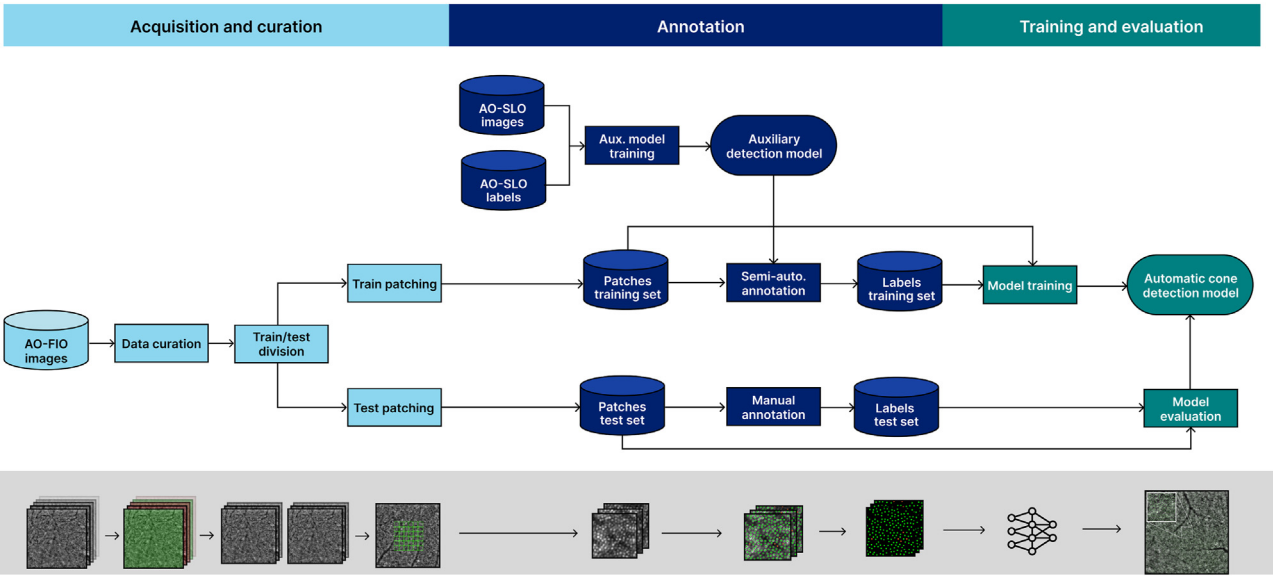

Figure 1. Project overview divided into 3 parts: image acquisition and curation, subdivision in patches and annotation, and model training/evaluation. AO-FIO = adaptive optics flood illumination ophthalmoscopy; AO-SLO = adaptive optics scanning laser ophthalmoscopy.

Data Annotation

To facilitate the annotation process, the images were first subdivided into patches of 128 × 128 pixels. The selection of patches differed between the training and test datasets. For the training dataset, the complete AO-FIO image was divided into patches. Since AO-FIO images sometimes exhibit lower quality or blurriness toward the edges of the image, the 4 outermost rows/columns on each side of the complete AO-FIO image were discarded, resulting in 36 different patches per training image, as shown in Figure 3 (left). Patches with vessel shadows covering more than half of the image were also discarded. In total, 625 patches were selected for the training set. For the test set, 3 patches per image were selected, following one of 4 different patterns: horizontal strip, vertical strip, or diagonal strip, as depicted in Figure 3 (right). All the sampling patterns of the test set had overlap between consecutive patches (the central patch overlapped with the 2 surrounding patches). Horizontal and vertical patterns had a 15% overlap between consecutive patches, while diagonal patterns had a 10% overlap. The varying sampling patterns with overlap were included to compute intragrader agreement. In total, 54 patches were selected for the test set.

The annotations were produced in a semiautomatic and manual way for the training and test sets, respectively. For the semi-automatic annotation, an auxiliary classic U-Net model was trained using a publicly available AO scanning laser ophthalmoscopy dataset,[28] as at the time of annotation, no AO-FIO datasets were

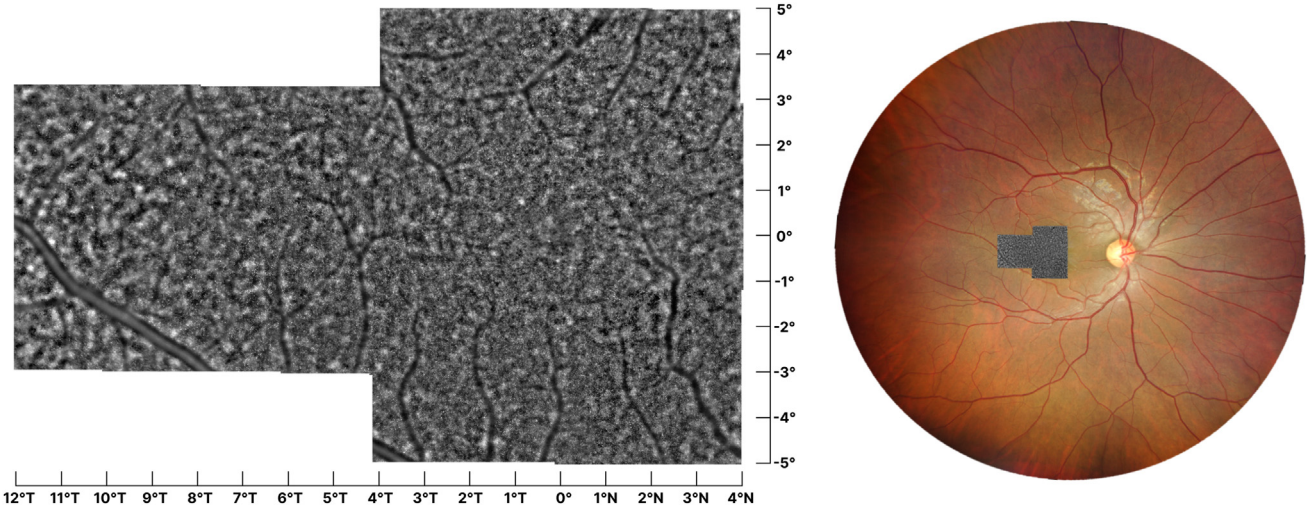

Figure 2. Adaptive optics flood illumination ophthalmoscopy montage resulting from the AO-VISION image acquisition protocol (left) and its colocalization on a 133° widefield color fundus image (right) acquired with the ZEISS CLARUS 500 (Zeiss).

Table 1. Demographics of the Training and Test Sets, Including the Number of Participants, Imaged Eyes, Total AO-FIO Images, and Age in Years

Dataset	# Participants	Eye (OD–OS)	# Images	Age (Mean ± SD)	Biological Sex (M-F)
Training	18	12–8	20	32.5 ± 12.4	6-12
Test	18	9–9	18	40.4 ± 15.8	11-7

AO-FIO = adaptive optics flood illumination ophthalmoscopy; F = female; M = male; SD = standard deviation.
OD represents the right eye, and OS represents the left eye.

publicly available. This model was used to generate predictions for all patches in the training set. Then the model output was corrected by grader G_1 or G_2, resulting in the reference standard for the training set. The corrections in the training set and manual annotations of the test set were carried out by placing one-pixel-wide dots at the central position of each cone photoreceptor visible in the patch. Two types of annotation were conducted based on the graders' confidence regarding the labeled structure as a cone: a green dot denoted a cone with high certainty, while an orange dot represented a cone with low certainty (e.g., dark cones). The criteria used to identify a cone in the image were as follows: (1) the structure has a round characteristic edge, (2) the structure has an intensity peak, and (3) the structure has a similar size and spacing compared with neighboring structures (smaller structures at larger eccentricities might be rod cells or cone cell outer segments). Any structure that met the 3 conditions was marked as green (certain). If only 2 conditions were met, the structure was marked as orange (uncertain). Otherwise, the structure was not marked. The data annotation/correction was performed using ITK-snap,[29] an open-source medical image visualization and annotation tool.

The test set was annotated by 4 graders (S.W., S.H., M.v.H., D.M.S.) with experience using the rtx1 retinal camera, including expertise in image acquisition and interpretation. Graders G_1 and G_2 worked at the same center C_1 and both had 3 months of experience. Grader G_3 from center C_2 had 1 year of experience, while grader G_4 from center C_3 had 8 years of experience with the rtx1 retinal camera. Figure 4 shows 4 images, each annotated by a different grader, along with an image displaying the differences between the annotations.

The intraobserver variability in the test set was computed for each of the 4 graders by comparing their manual annotations in the overlapped regions of the test set patches. For cell counting in AO-FIO images, a slight difference in marker position (e.g., one pixel off) was not penalized, since the device's resolution is not sufficient to show 2 different cells in such a close proximity. Thus, the metric proposed in the section "Evaluation Metrics," which accounts for a certain displacement of the marker relative to the center of the cell, was used for this comparison. Using this same metric, the interobserver variability was computed by comparing the manual annotations in the test set.

A fifth annotation was created by combining the manual annotations of the 4 graders, aiming for a more conservative set, i.e., a set including only those cells labeled either green or orange by multiple experts. A cell was added to the aggregated annotation if it met one of the 3 conditions: (1) labeled as green (certain) by $\geq$2 graders, (2) labeled as orange (uncertain) by $\geq$3 graders, or (3) labeled as green (certain) by 1 grader and as orange (uncertain) by $\geq$2 graders. The individual cell label position in the aggregated annotation was determined by computing the average position of the individual cell labels of

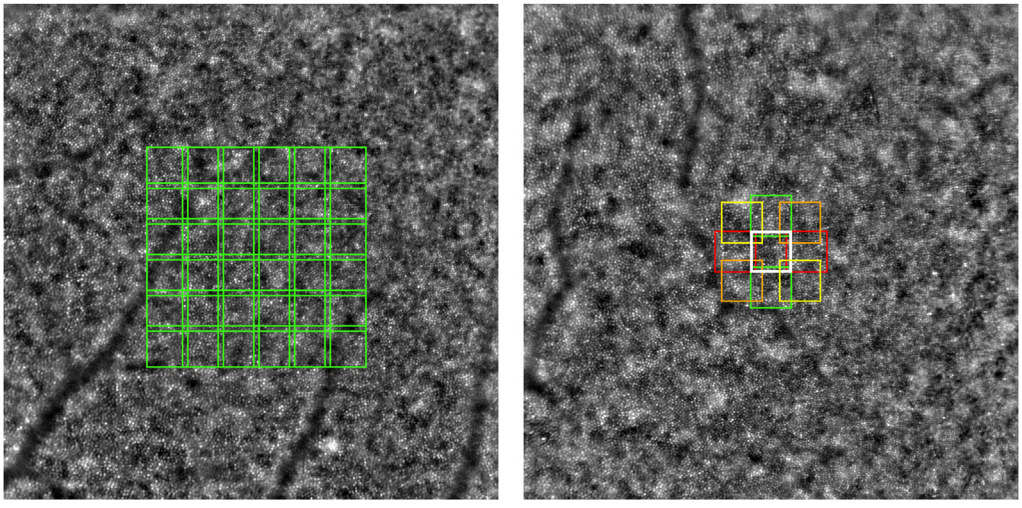

Figure 3. Adaptive optics flood illumination ophthalmoscopy 4° × 4° image with the representation of the patches selected for the training (left) and test (right) sets. Colors indicate different sampling patterns, with the white square representing the patch present in all of the 4 sampling patterns.

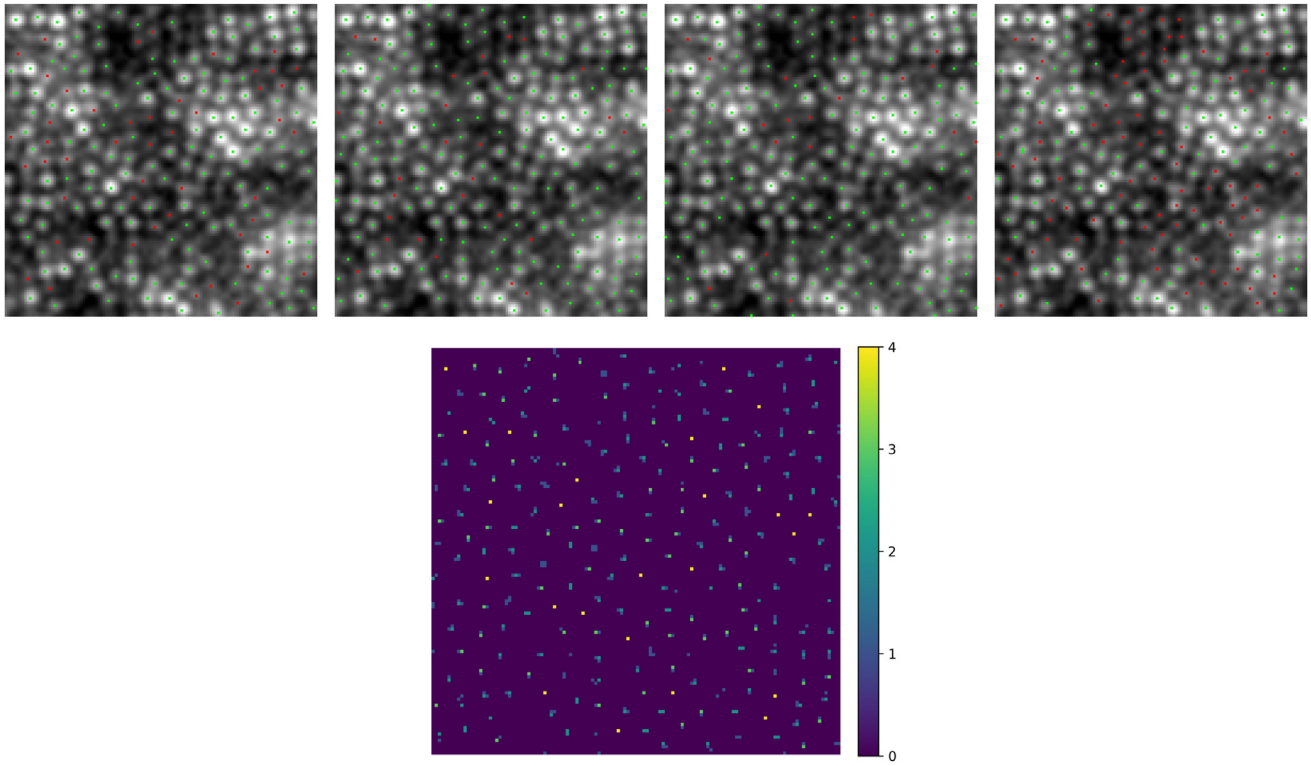

Figure 4. Adaptive optics flood illumination ophthalmoscopy patch (128 × 128 pixels) from an image acquired 3° inferior to the fovea, with cone photoreceptor cell annotations from graders 1 to 4 (upper row, left to right). Green denotes certain annotations, while orange denotes uncertain annotations. The second row shows the grading overlap, where yellow (4) indicates identical annotations across all graders, and purple (0) indicates no annotations.

the manual annotations. The AO-FIO data together with the annotations are available in the DataVerseNL repository.[30]

To overcome the limitation of a limited number of images in the test set, a more comprehensive experiment was conducted, involving all images of healthy controls in the AO-VISION database that clearly exhibited cone photoreceptors. In this larger experiment, the images were subdivided into 128 × 128 pixel patches using the same patching strategy as shown in Figure 3 (left), excluding the 4 rows and columns on each side of the image. Subsequently, the selected patches were processed using the AO-FIO ConeDetect. The density was calculated per patch using an axial length of 23.5 mm. For each image within the range of 2° to 10°T, the patch densities were averaged.

Model Architecture, Training, and Hyperparameter Optimization

The annotated masks in the training set underwent Gaussian blur transformation. This blurring process was implemented to address the imprecision associated with the human annotation process, mitigating potential inconsistencies and minor irregularities in the annotations. Also, it allows for a larger prediction target, which could, in turn, increase the training performance.[31] Next, both the image patches and their respective annotated masks were normalized between 0 and 1 to facilitate better convergence during model training.[32]

The deep learning architecture used for the identification of cones was based on the U-Net architecture.[33] The encoder−decoder structure incorporated a double convolutional block implemented at each stage. Each block comprised a 3×3 kernel convolutional layer, followed by batch normalization and ReLU activation, augmenting the features, and then a max pooling layer that facilitated dimension reduction, employing padding of 2 to ensure boundary consistency. Following the bottleneck between the encoder and decoder branches, the max pooling layer was replaced with a transposed convolutional layer, which had a stride of 2 and retrieved the original spatial resolution of the data. The last layer was a single convolutional layer with a 1 × 1 kernel, reducing the number of features to 1. The architecture could be changed by adjusting the number of features and layers, where each layer corresponded to a double convolutional block paired with either a pooling or transpose convolutional layer. An overview of the model architecture can be seen in Figure 5.

The parameters used to train the model were determined by a hyperparameter optimization method, the tree-structured Parzen estimator.[34] The tree-structured Parzen estimator algorithm systematically suggests new sets of hyperparameters for evaluation, taking into account the performance of previously tested configurations. This iterative process continues until the predefined stopping criterion of 100 iterations. The hyperparameter space covered different combinations of loss functions (L1, L2, Huber, and SmoothL1), preprocessing blurring kernel size (ranging from 1 × 1 to 17 × 17), batch sizes (8, 16, 32, 64), and adjustments in the architecture, namely the number of starting features (8, 16, 32, 64) and U-Net layers (2, 3, 4, 5). In each configuration, the Adam optimizer[35] was used, and

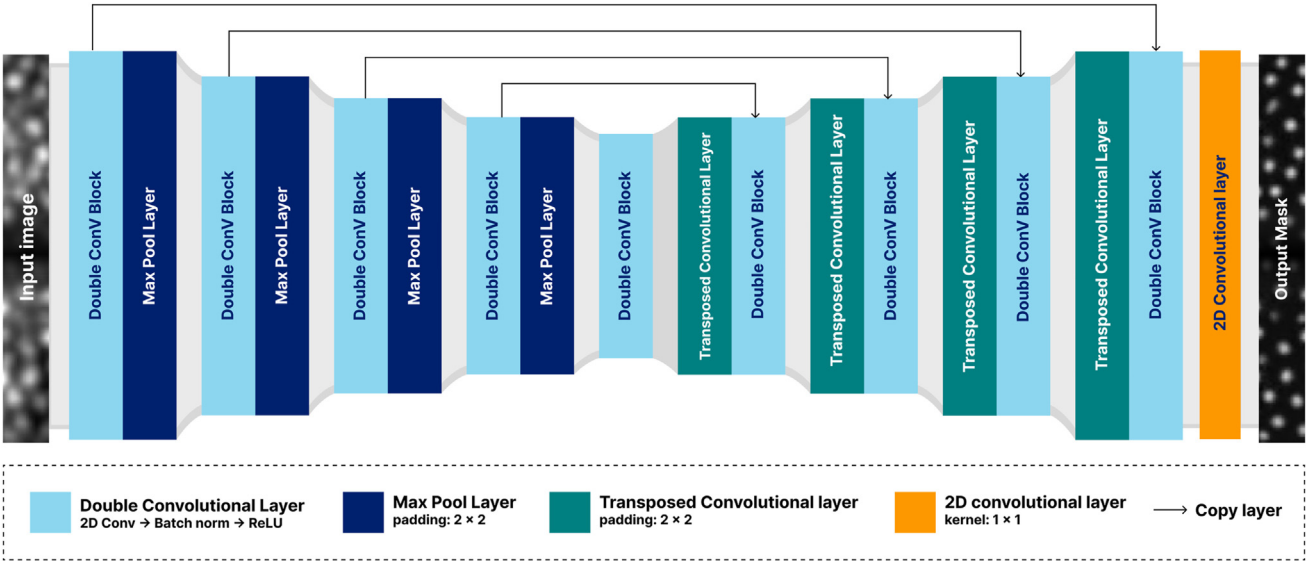

Figure 5. Overview of the U-Net architecture used in this study. 2D = 2-dimensional.

training was stopped when the F1 score on the validation fold did not improve within 15 epochs.

Throughout the training process, the model's performance was evaluated based on the metrics outlined in the section "Evaluation Metrics" using nine-fold cross-validation with a participant-based split. The weights of the model achieving the highest F1 score on the validation fold were saved. The model was trained using Python (v3.7.4) and PyTorch (v2.1.0) with Lightning (v2.1.2). The training was executed on an in-house GPU cluster. To maintain reproducibility of the experiments, a constant seed (s = 42) was kept for all randomized processes. The source code is available in the AO-FIO ConeDetect Gitlab repository.[36] The best hyperparameter configuration underwent retraining using leave-one-out cross-validation, and the best model (AO-FIO ConeDetect) was selected for further experiments and evaluations.

Evaluation Metrics

A metric adapted from the one proposed by Soltanian-Zadeh et al[37] was used for the cone detection performance evaluation. The output of the model (probability maps of the cells' positions) was postprocessed by applying Otsu thresholding[38] followed by 8-connectivity connected component analysis,[39] to separate each region produced by the thresholding in individual cells. Next, the segmented binary components were multiplied by the original input image. For each component, the highest relative intensity peak was retained as a central cell coordinate. In instances where multiple high-intensity peaks were identified, the point closest to the center location of the component was selected.

A predicted cone was deemed a true positive if the distance to the nearest annotated cone was less than the average cone radius observed in normal eyes. The number of true positives (N_{TP}) can be determined by the algorithm described in Algorithm 1. In this code, 2 sets of points were considered, namely $S_{\text{prediction}}$ and S_{target}. Both sets encompass coordinates denoted by (x_p, y_p) and (x_t, y_t), respectively. This particular metric can be seen as a closest point problem, resolved through a multidimensional binary search tree, commonly referred to as a KD-tree.[40] Both the literature[19,41] and empirical evidence in our dataset substantiate that a radius of 2.4 pixels (approximately 2 μm) as the appropriate distance to the nearest annotated cone. Hence, the distance between the predicted point and the closest target point was calculated using the KD-tree algorithm. If the calculated distance was <2.4 pixels, the corresponding predicted cell was recognized as a true positive. Subsequently, the point was removed from the set of target points. If the value was >2.4, no true positive was marked. This procedure was iterated for each point in the prediction set. The precision, recall, and F1 score were calculated using the count of true positives alongside the total number of cells in both the prediction and target sets.

Algorithm 1: True positive metric with defined radius.

$N_{tp} = 0$;
$radius = 2.4$;
Build a KDTree (KD_{target}) using S_{target};
while $S_{prediction} \neq 0$ **do**
  $(x_p, y_p) \leftarrow$ the first point in $S_{\text{prediction}}$;
  $(x_t, y_t) \leftarrow$ nearest point to (x_p, y_p) in KD_{target};
  distance $\leftarrow \sqrt{(x_p - x_t)^2 + (y_p - y_t)^2}$;
  if $distance \leq radius$ **then**
    $N_{tp} \leftarrow N_{tp} + 1$;
    Remove (x_t, y_t) from S_{target};
    Rebuild KD_{target} using new S_{target};
  end
  Remove (x_p, y_p) from $S_{\text{prediction}}$;
end
return N_{tp};

Results

For ease of interpretation, the results have been averaged into 3 groups: 2°N to 2°T, 3°T to 6°T, and 7°T to 10°T. The first range includes the foveal center and extends slightly into the parafoveal region. This area contains a high density of cone photoreceptors. The second range largely covers the parafovea, which still has a high density of cones but fewer than the fovea. Lastly, the third range extends into the perifoveal region, where the density of cone photoreceptors decreases further and more rod photoreceptors are present. Table 2 summarizes the number of images, patches, imaged eye, and ages in years per eccentricity range for the 18 participants in the test set.

Intragrader and Intergrader Agreement

The intragrader agreement within the overlapping regions of patches in the test set was analyzed. Each of the 3 patches within every AO-FIO image contained 2 overlapping areas, resulting in the evaluation of a total of 108 overlapping areas using the F1 score. For the assessment of intergrader agreement, 54 patches were compared between each pair of graders, also using the F1 score. The average values of the intragrader and intergrader scores are presented in Tables 3 and 4, respectively. The results show an average intragrader agreement of 0.85 ± 0.06 between 2°N and 2°T, followed by 0.83 ± 0.09 between 3 and 6°T, and 0.80 ± 0.10 between 7 and 10°T. The highest value was 0.90 ± 0.08 for the G2, C2 between 3 and 6°T, whereas the lowest value was 0.74 ± 0.13 for the G4, C3 between 7 and 10°T. The average intergrader agreement values for the 3 centers was 0.84 ± 0.05, 0.79 ± 0.05, and 0.76 ± 0.06 at 2°N−2°T, 3−6°T, and 7−10°T, respectively. The highest value, 0.85, was observed at 2°N−2°T between the graders G1−G2, G2−G3, and G1−G4. The agreement observed at 2°N−2°T between any of the centers C1, C2, and C3 was always ≥0.82. On the other hand, the lowest value was 0.73 ± 0.06 between G1, C1, and G4, C3 at 7−10°T.

Hyperparameter Optimization

The best combination of hyperparameters based on the tree-structured Parzen estimator algorithm achieved an F1 score of 0.89 ± 0.04, based on the mean F1 scores across all folds. The optimal configuration includes a 11 × 11 Gaussian blurring kernel, L1-loss function, batch-size of 64, U-Net starting features of 32, and 5 layers. Figure 6 illustrates an example of the predicted cones. The image showcases the model's performance in regions without and with vessel shadows. When the vessel shadow attenuates the signal significantly, no photoreceptors are detected; however, if the attenuation is less pronounced, cone photoreceptors can be identified.

Table 3. Intragrader Agreement for the 4 Graders at Eccentricity Ranges 2° Nasal (N) to 2° Temporal (T), 3° to 6°T, and 7° to 10°T

	2°N−2°T	3°−6°T	7°−10°T
G1	0.85 ± 0.06	0.84 ± 0.05	0.82 ± 0.05
G2	0.87 ± 0.05	0.90 ± 0.08	0.85 ± 0.07
G3	0.87 ± 0.05	0.84 ± 0.08	0.79 ± 0.08
G4	0.81 ± 0.05	0.77 ± 0.08	0.74 ± 0.13
Mean ± SD	0.85 ± 0.06	0.83 ± 0.09	0.80 ± 0.10

The last row denotes the mean and standard deviation (SD) for all graders.

Model Evaluation

The performance of the AO-FIO ConeDetect and AOdetect with no manual corrections was evaluated in comparison to the aggregated annotation (i.e., the annotation resulting from combining all manual annotations in the test set). The results can be seen in Table 5. The model exhibited an F1 score of 0.88 ± 0.04 for the range 2°N to 2°T, followed by 0.87 ± 0.03 for 3−6°T, and 0.82 ± 0.03 for 7−10°T. In contrast, AOdetect yielded F1 scores of 0.85 ± 0.05, 0.81 ± 0.03, and 0.69 ± 0.04 for the same eccentricities. Overall, the developed model presented higher F1 scores, with the largest difference observed in the eccentricity range of 7°−10°T when compared to AOdetect. Regarding the computation time, the model took on average 8.04 seconds to process a full rtx1 image (1500 × 1500 pixels) on an Intel Core i5 (3.40GHz) with 16GB of RAM, with no GPU acceleration.

The cone density of the 54 image patches of the test set was compared to the values reported in the literature.[24,42] The manually annotated patches, the AOdetect predicted patches—without manual correction—and the patches predicted by the model were transformed into cone density (cones/mm^2), using an axial length of 23.5 mm for the calculation. This particular value was selected due to the absence of axial length measurements from the healthy participants and the fact that 23.5 mm represents the

Table 2. Number of Participants, Imaged Eyes, Number of Images, Number of Patches, and Age in Years per Eccentricity Range in the Test Set

Eccentricity Range	# Participants	Eye (OD−OS)	# Images (#Patches)	Age (Mean ± SD)	Biological Sex (M-F)
2°N−2°T	7	3−4	7 (21)	40.0 ± 16.7	4-3
3°T−6°T	5	2−3	5 (15)	43.4 ± 18.4	4-1
7°T−10°T	6	4−2	6 (18)	38.5 ± 15.0	3-3
Total	18	9−9	18 (54)	40.4 ± 15.8	11-7

F = female; M = male; N = nasal; SD = standard deviation; T = temporal.
OD represents the right eye, and OS represents the left eye.

Table 4. Intergrader Agreement for the 4 Graders at Eccentricity Ranges 2° Nasal (N) to 2° Temporal (T), 3° to 6°T, and 7° to 10°T

	2°N–2°T	3°–6°T	7°–10°T
G1 vs. G2	0.85 ± 0.04	0.84 ± 0.03	0.80 ± 0.03
G1 vs. G3	0.82 ± 0.05	0.81 ± 0.03	0.76 ± 0.04
G1 vs. G4	0.85 ± 0.04	0.77 ± 0.04	0.73 ± 0.06
G2 vs. G3	0.85 ± 0.05	0.83 ± 0.04	0.81 ± 0.03
G2 vs. G4	0.84 ± 0.05	0.79 ± 0.05	0.74 ± 0.06
G3 vs. G4	0.82 ± 0.07	0.75 ± 0.05	0.75 ± 0.07
Mean ± SD	0.84 ± 0.05	0.79 ± 0.05	0.76 ± 0.06

The last row denotes the mean and standard deviation (SD) for all combinations.

Table 5. Comparison of F1 Score Between the AO-FIO ConeDetect and AOdetect at Eccentricity Ranges 2° Nasal (N) to 2° Temporal (T), 3° to 6°T, and 7° to 10°T

	2°N–2°T	3°–6°T	7°–10°T
AO-FIO ConeDetect			
Precision	0.88 ± 0.05	0.84 ± 0.03	0.76 ± 0.04
Recall	0.88 ± 0.04	0.90 ± 0.03	0.91 ± 0.03
F1 score	0.88 ± 0.04	0.87 ± 0.03	0.82 ± 0.03
AOdetect (uncorrected)			
Precision	0.83 ± 0.07	0.75 ± 0.05	0.57 ± 0.05
Recall	0.88 ± 0.04	0.88 ± 0.02	0.87 ± 0.04
F1 score	0.85 ± 0.05	0.81 ± 0.03	0.69 ± 0.04

AO-FIO = adaptive optics flood illumination ophthalmoscopy.

average of the reported range from 22 to 25 mm.[43] Each 128 × 128 pixel patch is approximately 98 × 98 μm. The results for manual annotation and algorithm-predicted densities compared with literature are presented in Figure 7A.

The results indicate a decrease in cone density for larger eccentricities, aligning with existing literature. Muthiah et al[42] reported a declining cone density, ranging from 26 500 cones/mm^2 at 2°T to 11 200 cones/mm^2 at 7°T, based on manually annotated images. Legras et al[24] also observed a decrease, from 31 437 cones/mm^2 at 2°T to 17 734 cones/mm^2 at 5°T. In this study, lower values are reported for these ranges, as shown in Figure 7A and Table 6. The mean error difference for AO-FIO ConeDetect is consistently lower than for AOdetect for all studied eccentricities and is similar to the difference between individual annotations and the aggregated set (<10% for 2°–6°T and 20% between 7° and 10°T).

The results, involving all images of healthy controls from the AO-VISION database, divided into 2 age groups (18–30 years and >50 years old), are shown in Figure 7B. The results demonstrate a decrease in cell density for larger eccentricities in both age groups, consistent with previous experiments and literature. However, cone density at eccentricities between 2° and 4° was lower compared with the literature. Additionally, the results indicate a decrease in cell density for older participants, particularly between 2° and 5°T.

To assess the impact of different sampling patterns on cell density estimation, a comparison of 3 sampling patterns was conducted, as illustrated in Figure 8. The findings indicate that avoiding borders or vessel shadows leads to higher observed cell density.

Discussion

Adaptive optics flood illumination ophthalmoscopy is an imaging technology that overcomes the inherent limitations of traditional retinal imaging, offering an unprecedented

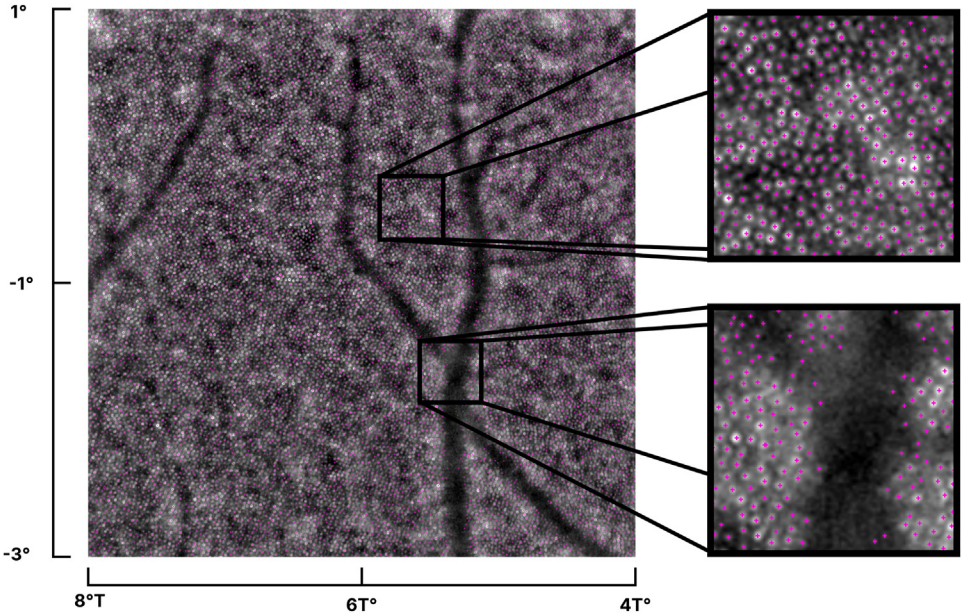

Figure 6. Example of the AO-FIO ConeDetect prediction on a healthy individual imaged at 6° temporal, with 2 regions illustrating the prediction on segments without and with vessel shadows. AO-FIO = adaptive optics flood illumination ophthalmoscopy.

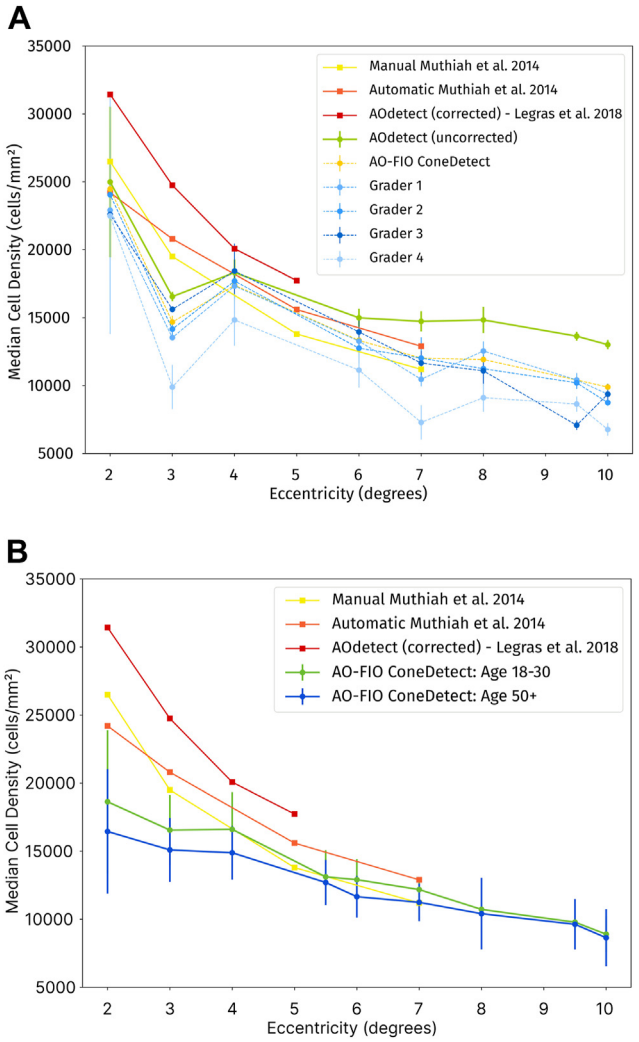

Figure 7. Cell density (cones/mm^2) at various central image eccentricities (degrees). **A**, Median cell density calculated for the 54 image patches from the test set, focusing on eccentricities ranging between 2 and 10° temporal, and compared with values reported in the literature. **B,** Median cell density calculated for 819 AO-FIO images divided by age group, focusing on eccentricities ranging between 2 and 10° temporal, and compared with values reported in the literature. AO-FIO = adaptive optics flood illumination ophthalmoscopy.

view into the cellular and vascular architecture of the retina. Adaptive optics correction will certainly become an integral part of imaging modalities for examining the retina in ophthalmology in the upcoming years.

In this study, we introduced a deep learning model, AO-FIO ConeDetect, for the automated detection of cone photoreceptor cells in AO-FIO images. The model's performance was compared with manual annotations from 3 medical centers. To the best of our knowledge, this is the first work to present a multicenter intragrader and intergrader agreement analysis of cell detection in AO-FIO images. Intragrader agreement analysis showed that graders are often more certain at eccentricities closer to the fovea and less certain in more peripheral images. This may be explained by the decrease in the number of cone photoreceptor cells as a function of eccentricity and the increase in the number of rod cells. The AO-FIO images can show observable differences in healthy individuals, such as those resulting from the light reaching the cone outer segment at different angles or with different intensities due to the morphology of the retinal tissues. These differences in appearance contribute to the increase in uncertainty in manual annotations. Importantly, imaging cones at the fovea is often not possible due to both the limited resolution of the device (approximately 2 μm) and the dense packing of cone cells in this region, which hinders the alignment of the outer and inner segments, resulting in a blurry foveal spot rather than clear visualization. This suggests that an increase in uncertainty would be expected in these regions. However, the selection criteria for the test set included that the images offered a good visualization of individual cells. In consequence, none of the images with fixation coordinates on the center of the fovea were selected (0°, 0°). For the lowest eccentricity group, the test set images included were centered either at 2°N or 2°T, and respective patches were also centered, as shown in Figure 3. Therefore, all patches in the test set had well-resolved photoreceptors.

Intragrader agreement was slightly higher than intergrader agreement, with higher uncertainty observed between 7° and 10°T. This indicates that the difference across institutions is similar to intragrader variability. Despite different levels of expertise among the centers in this study, the knowledge of what shall be considered a cone photoreceptor cell is somehow consistent across centers, ranging from 0.9 to 0.74 in intra-agreement F1 score and from 0.85 to 0.74 in interagreement F1 score. However, it is noteworthy that graders from C1 consistently annotated more cells than the aggregated annotation, while the grader from C3 consistently annotated fewer cells, except at the eccentricity of 2°. This underscores the importance of establishing consensus and standard guidelines for annotating these images. Only by building and sharing knowledge across institutions can we aim to improve both intra- and inter-agreements. These findings underscore the need for consensus and standardized guidelines for annotating and interpreting these images. It is also crucial to recognize that these F1 scores are based on annotations from healthy volunteers. Annotating cone photoreceptors in images with retinal diseases is inherently more challenging and will most likely result in lower intragrader and intergrader agreements. This limitation highlights the current challenges faced by AO-FIO imaging and underscores the need for future research and development to address these issues, particularly in pathological conditions.

Nevertheless, building on the existing knowledge and limitations, it was possible to develop a deep learning model for the automatic detection of photoreceptor cone cells. The performance of the model is comparable to the reference standard generated from the aggregated annotation of the 4 graders, with the F1 score ranging from 0.88 to 0.82 from the center to the periphery. The model achieved an automated detection similar to that of human experts over regions of interest of 128 × 128 pixels and can be extended to large regions captured with AO-FIO imaging. The

Table 6. Median Cell Density per 1000 Cones/mm^2 Assessed in Manual Annotations, the Developed Model, and AOdetect on the Test Set

	2°T	3°T	4°T	6°T
Grader 1	22.9 ± 7.4 | 2.8%	13.5 ± 0.1| 0.8%	17.3 ± 2.0 | 2.1%	13.3 ± 1.1 | 9.9%
Grader 2	24.1 ± 6.6 | 7.9%	14.2 ± 0.5 | 5.4%	17.7 ± 1.3 | 4.3%	12.6 ± 1.1 | 5.6%
Grader 3	22.6 ± 6.4 | 1.4%	15.6 ± 0.2 | 16.3%	18.4 ± 2.0 | 8.6%	14.0 ± 0.9 | 15.5%
Grader 4	22.5 ± 8.7 | 0.9%	9.9 ± 1.6 | −26.4%	14.8 ± 1.9 | −12.6%	11.1 ± 1.3 | −7.8%
Aggregated annotation	22.3 ± 7.1	13.4 ± 0.3	17.0 ± 1.7	12.1 ± 0.9
AO-FIO ConeDetect	24.5 ± 6.0 | 9.8%	14.7 ± 0.5 | 9.3%	17.4 ± 1.4 | 2.5%	13.3 ± 1.0 | 10.3%
AOdetect (uncorrected)	25.0 ± 5.5 | 12.1%	16.6 ± 0.3 | 23.3%	18.3 ± 0.9 | 8.0%	15.0 ± 0.7 | 24.1%
	7°T	**8°T**	**9.5°T**	**10°T**
Grader 1	10.5 ± 0.5 | 3.1%	12.5 ± 0.7 | 21.1%	10.4 ± 0.5 | 19.0%	9.4 ± 0.4 | 9.8%
Grader 2	12.0 ± 1.5 | 18.5%	11.2 ± 0.1 | 8.5%	10.2 ± 0.4 | 16.7%	8.7 ± 0.2 | 2.4%
Grader 3	11.7 ± 0.9 | 14.9%	11.1 ± 1.0 | 7.0%	7.1 ± 0.4 | −19.0%	9.4 ± 0.8 | 9.8%
Grader 4	7.3 ± 1.3 | −28.2%	9.1 ± 1.0 | −12.1%	8.6 ± 0.6 | −1.2%	6.8 ± 0.5 | −20.7%
Aggregated annotation	10.2 ± 0.8	10.4 ± 0.8	8.7 ± 0.2	8.5 ± 0.3
AO-FIO ConeDetect	12.0 ± 1.0 | 18.5%	11.9 ± 1.0 | 15.1%	10.4 ± 0.0 | 19.0%	9.9 ± 0.1 | 15.8%
AOdetect (uncorrected)	14.7 ± 0.7 | 45.1%	14.8 ± 1.0 | 43.2%	13.6 ± 0.3 | 56.0%	13.0 ± 0.3 | 52.4%

AO-FIO = adaptive optics flood illumination ophthalmoscopy; T = temporal.
Results are displayed for eccentricities spanning 2 to 10°T. The percentage value represents the deviation from the aggregated annotation.

implemented batch prediction approach can be run for any image regardless of its size, be it a simple 4° × 4° image or a full montage.

As mentioned previously, only 2 other tools for cell analysis in AO-FIO data exist. The software facilitated by the manufacturer, AOdetect, is intended as an aid for annotating the cone cells and not as a fully automatic tool. Therefore, it is meant to be used in a semiautomated manner (the software provides a first estimation that should be reviewed and corrected by the clinician). However, this process is time consuming and impractical for image montages and large-scale experiments, such as those described in this article. As a consequence, in this work, only the automatic results are reported, without the manual correction step. Therefore, our AOdetect results should not be compared with other papers in the literature that use the tool in the intended, semiautomatic manner.[23,24] Comparisons with the other available software (MATADOR) were not conducted because it was not possible to export the predicted cone coordinates. Furthermore, due to its

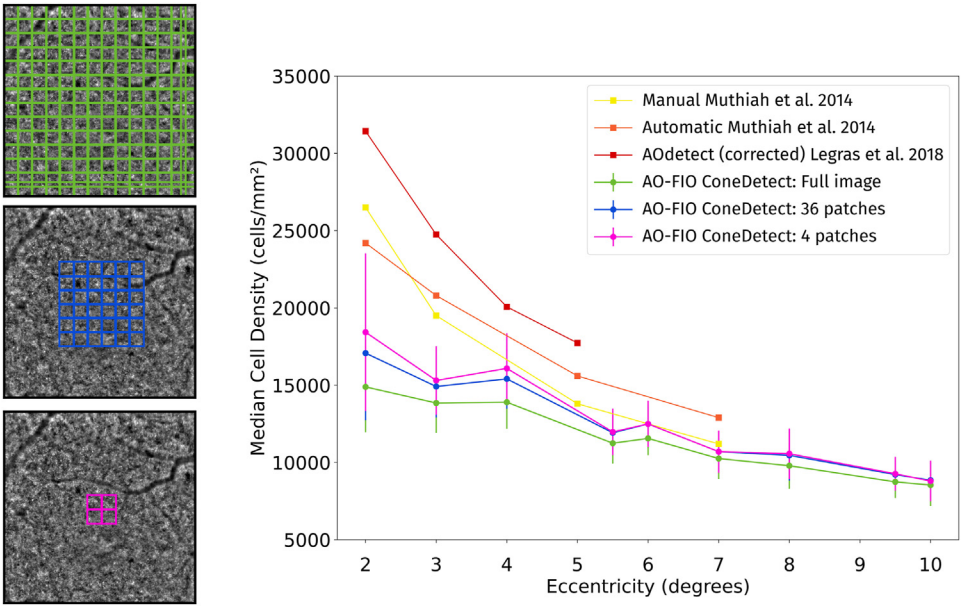

Figure 8. Median cell density calculated for 819 AO-FIO images for 3 different sampling patterns: full image (196 patches), the training dataset pattern (36 patches), and 4 patches located in the center of the image. AO-FIO = adaptive optics flood illumination ophthalmoscopy.

closed-software nature, it was not possible to modify the tool to enable the required export functionality.

In this fully automatic context, the model performed better than AOdetect at higher eccentricities. This points out how predictions in the peripheral regions should be reviewed more carefully. As shown in Figure 7A, the graders, the model, and AOdetect estimated a similar number of cells for smaller eccentricities, which changed for larger eccentricities with AOdetect having more false positives. This is in agreement with previous studies that reported how AOdetect initial predictions need more manual corrections at higher eccentricities.[25] However, analyses in the peripheral areas are particularly relevant for some diseases, such as retinitis pigmentosa, that expand from the periphery to the center.[44] The model investigated here overcomes 2 limitations of AOdetect, as it can provide less false positives at high eccentricities and over larger areas, without the need for manual correction to facilitate large-scale studies.

Figure 7 illustrates a decrease in estimated cell density at 3°T relative to 4°T or existing literature findings. Nonetheless, the model's predictions align with both manual annotations and AOdetect's automated predictions. A likely reason for this decrease could be the limited number of image patches at 3°T, with only 3 image patches included in the test set, making it susceptible to outlier effects. Visual examinations confirm the high quality of the images, with no visible causes for the reduced cell density. This underscores the importance of establishing a comprehensive, normative database to accurately determine expected density values in a typical population.

We have used the model to compare the cone densities between a group of healthy individuals aged 18 to 30 years and one of individuals aged ≥50 years (Fig 7B). The results show a higher cell density for the younger participants, especially at lower eccentricities, highlighting the sensitivity of the model for the diagnosis of subtle changes that may occur in the retina at the photoreceptor level. These results are globally lower than those shown in Figure 7A. As shown in Figure 8, the cell density values for an image significantly increase if we only include the central part of the image. The 36 patches included in the training set sampling pattern depicted in Figure 7A represent the $2^\circ \times 2^\circ$ at the center of the image, and hence the discrepancy with Figure 7B, which includes the complete images. One reason for this is that complete images are likely to include vessel shadows, which cause underestimated values, and these are more frequent in the edges of the image due to how we selected our dataset excluding the images with major vessel shadows. In studies using AOdetect, the values comparable with histology were achieved when manually positioning the small regions of interest to avoid vessel shadows.[23,24] The appropriate exclusion of vessel shadows is crucial, as their presence can significantly alter cone density estimates, particularly in areas with larger vessels. Furthermore, the gradient of cone density with eccentricity, which is particularly steep closer to the fovea, also impacts the values. This is in line with previous studies based on conventional cone detection methods without manual correction that reported underestimated density values when increasing the sampling window size.[45–47] This highlights the importance of developing models in future works to restrict the area of analysis, excluding vessel shadows or regions that do not have enough image quality. Incorporating peripheral regions may lead to different results due to varying image quality, which could be a critical consideration for future research in automatic cone detection. Additionally, more appropriate outputs for density values and variations, such as density maps that display local variations or density values computed in smaller regions, could help reduce underestimation when analyzing large areas.

The results in Figure 7 also show that the median cell density measurements are slightly below those reported by Legras et al[24] and are in agreement with those reported by Muthiah et al manual method.[42] This might be explained by the methods for estimating density values, such as sampling window size (this work used a similar size as Muthiah et al but larger than Legras et al), the inclusion or exclusion of vessel shadows, and the method for calculating density (Muthiah et al uses a similar approach to this work, while Legras et al uses a similar approach to AOdetect, based on Voronoi cells). Additionally, axial length has been reported as a factor contributing to interindividual variability in cone density in healthy populations.[24] Legras et al compensated for real axial length values, whereas our work used an estimate. Nevertheless, future work could present the results as cones per degree,[3] which would mitigate the need for axial length measurements. This approach would standardize density calculations across individuals by accounting for retinal area in angular terms rather than relying on axial length estimations.

It is also essential to note that this study only included photoreceptor layer imaging of healthy volunteers. Adaptive optics flood illumination ophthalmoscopy images can differ significantly in pathological conditions, and this algorithm has yet to be tested on images from patients with retinal diseases. Future work will be necessary to validate and adapt the algorithm for these more complex scenarios. Moreover, further research should be performed in building normative databases for AO-FIO imaging. Although we studied variability across ages, which demonstrate slight changes in photoreceptor density and image quality, further studies and validation should also be extended to various patient populations. Furthermore, the analysis of such data should also be correlated with and supported by histological and multimodal imaging data.

This study presents a deep learning model for the automated detection of cone photoreceptor cells in AO-FIO images. Adaptive optics flood illumination ophthalmoscopy ConeDetect's performance, comparable to human experts, demonstrates its potential utility in overcoming the current limitations of existing methodologies, particularly in the peripheral retina. The intra- and interagreement analysis presented in this research underscores areas for improvement as well as the need for established protocols when annotating AO-FIO images. This highlights the importance of sharing knowledge among institutions to improve the levels of agreement.

Footnotes and Disclosures

Originally received: June 5, 2024.
Final revision: November 15, 2024.
Accepted: December 6, 2024.
Available online: December 12, 2024. Manuscript no. XOPS-D-24-00172.

[1] Biomedical Imaging Group Rotterdam, Department of Radiology & Nuclear Medicine, Erasmus MC, Rotterdam, The Netherlands.

[2] Leiden Institute of Advanced Computer Science, Leiden University, Leiden, The Netherlands.

[3] Department of Ophthalmology, Erasmus MC, Rotterdam, The Netherlands.

[4] Department of Epidemiology, Erasmus MC, Rotterdam, The Netherlands.

[5] Department of Ophthalmology, Ghent University Hospital, Ghent, Belgium.

[6] Department of Head & Skin, Ghent University, Ghent, Belgium.

[7] Centre for Ophthalmology and Visual Sciences, The University of Western Australia, Perth, Australia.

[8] Ophthalmology, Department of Surgery, University of Melbourne, East Melbourne, Victoria, Australia.

[9] The Rotterdam Ophthalmic Institute, The Rotterdam Eye Hospital, Rotterdam, The Netherlands.

[10] Department of Clinical Genetics, Erasmus MC, Rotterdam, The Netherlands.

[11] Department of Ophthalmology, Radboud University Medical Center, Nijmegen, The Netherlands.

[12] Institute of Molecular and Clinical Ophthalmology, University of Basel, Basel, Switzerland.

[13] Imagine Eyes, Orsay, France.

*D.A.J. and L.S.B. contributed equally to this work.

The results in this study were partially presented and discussed at ARVO Annual Meeting, Seattle, USA.[1]

Disclosure(s):

All authors have completed and submitted the ICMJE disclosures form.

The authors made the following disclosures:

M.D.: Grants − Imagine Eyes, Orsay, France (employee).

N.C.: Grants − Imagine Eyes, Orsay, France (employee and shareholder).

This work was supported by Health Holland, Top Sector Life Sciences & Health under grant agreement no. EMCLSH22014 (AO-VISION).

Support for Open Access publication was provided by Erasmus MC.

HUMAN SUBJECTS: Human subjects were included in this study. This research is part of the AO-VISION study (MEC−2022−0495) that received approval from the Medical Ethics Committee at Erasmus MC (METC Erasmus Medisch Centrum Rotterdam). A signed consent was obtained from each participant, who was informed about the study and the intended application of their data. Before any analysis, the data were anonymized. This research adhered to the tenets of the Declaration of Helsinki.

No animal subjects were used in this study.

Author Contributions:

Conception and design: Wooning, Roshandel, Pelt, Chateau, van Walsum, Andrade De Jesus, Sanchez Brea

Data collection: Wooning, Heutinck, Liman, Hennekam, Andrade De Jesus, Sanchez Brea

Analysis and interpretation: Wooning, Heutinck, Hennekam, van Haute, Sampson, Roshandel, van den Born, Thiadens, Durand, Andrade De Jesus, Sanchez Brea

Obtained funding: Klaver, Chateau, van Walsum, Andrade De Jesus, Sanchez Brea. Study was performed as part of regular employment duties at Erasmus MC. No additional funding was provided.

Overall responsibility: Wooning, Heutinck, van Haute, van den Broeck, Leroy, Sampson, Roshandel, Chen, Pelt, van den Born, Klaver, Thiadens, Durand, Chateau, van Walsum, Andrade De Jesus, Sanchez Brea

Abbreviations and Acronyms:
AO = adaptive optics; **AO-FIO** = adaptive optics flood illumination ophthalmoscopy; **N** = nasal; **T** = temporal.

Keywords:
Adaptive optics flood illumination ophthalmoscopy, Retinal imaging, Cone photoreceptor cells, Automated detection, Cone mosaic analysis.

Correspondence:
Danilo Andrade De Jesus, PhD, Department of Radiology & Nuclear Medicine, Erasmus Medical Center, Dr. Molewaterplein 40, Na2512, Rotterdam 3015 GD, The Netherlands. E-mail: d.andradedejesus@erasmusmc.nl.

References

1. Andrade De Jesus D, Wooning S, van Haute M, et al. Automated segmentation of cone photoreceptors in AO-FIO: a multi-center study. *Invest Ophthalmol Vis Sci*. 2024;65:1419.
2. Babcock HW. The possibility of compensating astronomical seeing. *Publ Astron Soc Pac*. 1953;65:229−236.
3. Lombardo M, Parravano M, Serrao S, et al. Investigation of adaptive optics imaging biomarkers for detecting pathological changes of the cone mosaic in patients with type 1 diabetes mellitus. *PLoS One*. 2016;11:e0151380.
4. McIlwaine G, Csincsik L, Coey R, et al. Reduced cone density is associated with multiple sclerosis. *Ophthalmol Sci*. 2023;3:100308.
5. Paques M, Meimon S, Rossant F, et al. Adaptive optics ophthalmoscopy: application to age-related macular degeneration and vascular diseases. *Prog Retin Eye Res*. 2018;66:1−16.
6. Georgiou M, Kalitzeos A, Patterson EJ, et al. Adaptive optics imaging of inherited retinal diseases. *Br J Ophthalmol*. 2018;102:1028−1035.
7. Torm MEW, Pircher M, Bonnin S, et al. Detection of capillary abnormalities in early diabetic retinopathy using scanning laser ophthalmoscopy and optical coherence tomography combined with adaptive optics. *Sci Rep*. 2024;14:13450.
8. Zhang Y, Cense B, Rha J, et al. High-speed volumetric imaging of cone photoreceptors with adaptive optics spectral-domain optical coherence tomography. *Opt Express*. 2006;14:4380−4394.
9. Roorda A, Romero-Borja F, Donnelly Iii W, et al. Adaptive optics scanning laser ophthalmoscopy. *Opt Express*. 2002;10:405−412.
10. Shirazi MF, Lefaudeux N, Lefaudeux N, et al. Multi-modal and multi-scale clinical retinal imaging system with pupil and retinal tracking. *Sci Rep*. 2022;12:9577.
11. Zacharria M, Lamory B, Chateau N. New view of the eye. *Nat Photonics*. 2011;5:24−26.
12. Szewczuk A, Zaleska-Zmijewska A, Dziedziak J, Szaflik JP. Clinical application of adaptive optics imaging in diagnosis,

management, and monitoring of ophthalmological diseases: a narrative review. *Med Sci Monit*. 2023;29:e941926.
13. Takagi S, Mandai M, Gocho K, et al. Evaluation of transplanted autologous induced pluripotent stem cell-derived retinal pigment epithelium in exudative age-related macular degeneration. *Ophthalmol Retin*. 2019;3:850−859.
14. Bakker E, Dikland FA, van Bakel R, et al. Adaptive optics ophthalmoscopy: a systematic review of vascular biomarkers. *Surv Ophthalmol*. 2022;67:369−387.
15. Kubota D, Matsumoto K, Hayashi M, et al. High-resolution photoreceptor imaging analysis of patients with autosomal dominant retinitis pigmentosa (adrp) caused by hk1 mutation. *Ophthalmic Genet*. 2020;41:629−638.
16. Ziccardi L, Giannini D, Lombardo G, et al. Multimodal approach to monitoring and investigating cone structure and function in an inherited macular dystrophy. *Am J Ophthalmol*. 2015;160:301−312.
17. Nakanishi A, Ueno S, Hayashi T, et al. Changes of cone photoreceptor mosaic in autosomal recessive bestrophinopathy. *Retina*. 2020;40:181−186.
18. Heutinck P, Andrade De Jesus D, Sanchez Brea L, et al. Parafoveal cone loss in inherited retinal dystrophy patients using the rtx1 adaptive optics retinal camera. *Invest Ophthalmol Vis Sci*. 2023;64:1063.
19. Liu J, Jung H, Dubra A, Tam J. Cone photoreceptor cell segmentation and diameter measurement on adaptive optics images using circularly constrained active contour model. *Invest Ophthalmol Vis Sci*. 2018;59:4639−4652.
20. Cunefare D, Fang L, Cooper RF, et al. Open source software for automatic detection of cone photoreceptors in adaptive optics ophthalmoscopy using convolutional neural networks. *Sci Reports*. 2017;7:6620.
21. Chen Y, He Y, Wang J, et al. Automated cone photoreceptor cell segmentation and identification in adaptive optics scanning laser ophthalmoscope images using morphological processing and watershed algorithm. *IEEE Access*. 2020;8:105786−105792.
22. Valterova E, Unterlauft JD, Francke M, et al. Comprehensive automatic processing and analysis of adaptive optics flood illumination retinal images on healthy subjects. *Biomed Opt Express*. 2023;14:945−970.
23. Suzuki K, Gocho K, Akeo K, et al. High-resolution retinal imaging reveals preserved cone photoreceptor density and choroidal thickness in female carriers of choroideremia. *Ophthalmic Surg Lasers Imaging Retina*. 2019;50:76−85.
24. Legras R, Gaudric A, Woog K. Distribution of cone density, spacing and arrangement in adult healthy retinas with adaptive optics flood illumination. *PLoS One*. 2018;13:e0191141.
25. Woog K, Legras R. Distribution of mid-peripheral cones in emmetropic and myopic subjects using adaptive optics flood illumination camera. *Ophthalmic Physiol Opt*. 2019;39:94−103.
26. Liu X, Song L, Liu S, Zhang Y. A review of deep-learning-based medical image segmentation methods. *Sustainability*. 2021;13:1224.
27. Zaleska-Zmijewska A, Wawrzyniak ZM, DaÎbrowska A, et al. Adaptive optics (rtx1) high-resolution imaging of photoreceptors and retinal arteries in patients with diabetic retinopathy. *J Diabetes Res*. 2019;2019.
28. Chiu SJ, Lokhnygina Y, Dubis AM, et al. Automatic cone photoreceptor segmentation using graph theory and dynamic programming. *Biomed Opt Express*. 2013;4:924−937.
29. Yushkevich PA, Piven J, Hazlett HC, et al. User-guided 3D active contour segmentation of anatomical structures: significantly improved efficiency and reliability. *Neuroimage*. 2006;31:1116−1128.
30. Wooning S, Heutinck P, Liman K, et al. Replication data for: automated cone photoreceptors detection in adaptive optics flood-illumination. *Ophthalmoscopy*. 2024. https://doi.org/10.34894/2GXEDZ.
31. Shiraz A, Egawa N, Pelt DM, et al. Cervical cell lift: a novel triage method for the spatial mapping and grading of precancerous cervical lesions. *EBioMedicine*. 2022;82:104157.
32. Ioffe S, Szegedy C. Batch normalization: accelerating deep network training by reducing internal covariate shift. In: *International conference on machine learning*. Lille, France: pmlr; 2015:448−456.
33. Ronneberger O, Fischer P, Brox T. U-net: convolutional networks for biomedical image segmentation. In: Navab N, Hornegger J, Wells WM, Frangi AF, eds. *Medical Image Computing and Computer-Assisted Intervention − MICCAI 2015*. Cham: Springer International Publishing; 2015:234−241.
34. Bergstra J, Bardenet R, Bengio Y, Kégl B. Algorithms for hyper-parameter optimization. *Adv Neural Inf Process Syst*. 2011;24.
35. Kingma DP, Ba J. Adam: A method for stochastic optimization. *arXiv*. 2014. https://doi.org/10.48550/arXiv.1412.6980.
36. Wooning S, Sanchez Brea L, Andrade de jesus D. AO-FIO ConeDetect. https://gitlab.com/radiology/eye/ao-vision/ao-fio-conedetect.git; 2024. Accessed May 6, 2024.
37. Soltanian-Zadeh S, Liu Z, Liu Y, et al. Deep learning-enabled volumetric cone photoreceptor segmentation in adaptive optics optical coherence tomography images of normal and diseased eyes. *Biomed Opt Express*. 2023;14:815−833.
38. Otsu N. A threshold selection method from gray-level histograms. *IEEE Trans Syst Man Cybern*. 1979;9:62−66.
39. Bolelli F, Allegretti S, Baraldi L, Grana C. Spaghetti labeling: directed acyclic graphs for block-based connected components labeling. *IEEE Trans Image Process*. 2020;29:1999−2012.
40. Bentley JL. Multidimensional binary search trees used for associative searching. *Commun ACM*. 1975;18:509−517.
41. Scoles D, Sulai YN, Langlo CS, et al. In vivo imaging of human cone photoreceptor inner segments. *Invest Ophthalmol Vis Sci*. 2014;55:4244−4251.
42. Muthiah MN, Gias C, Chen FK, et al. Cone photoreceptor definition on adaptive optics retinal imaging. *Br J Ophthalmol*. 2014;98:1073−1079.
43. Bhardwaj V, Rajeshbhai GP. Axial length, anterior chamber depth-a study in different age groups and refractive errors. *J Clin Diagn Res*. 2013;7:2211.
44. Menghini M, Cehajic-Kapetanovic J, MacLaren RE. Monitoring progression of retinitis pigmentosa: current recommendations and recent advances. *Expert Opin Orphan drugs*. 2020;8:67−78.
45. Lombardo M, Serrao S, Ducoli P, Lombardo G. Influence of sampling window size and orientation on parafoveal cone packing density. *Biomed Opt Express*. 2013;4:1318−1331.
46. Feng S, Gale MJ, Fay JD, et al. Assessment of different sampling methods for measuring and representing macular cone density using flood-illuminated adaptive optics. *Invest Ophthalmol Vis Sci*. 2015;56:5751−5763.
47. Zaleska-Zmijewska A, Wawrzyniak ZM, Ulińska M, et al. Human photoreceptor cone density measured with adaptive optics technology (rtx1 device) in healthy eyes: standardization of measurements. *Medicine*. 2017;96:e7300.